Rijks*universiteit* Groningen

Faculteit der Wiskunde en Natuurkunde, Zernike Institute for Advanced Materials

Onderzoeksgroep: Nanostructured Materials and Interfaces

Switching Casimir forces with Phase Change Materials

Master thesis by:
Oleksandr Shpak

Supervisors: Dr. G. Palasantzas

Referent: Dr.ir. B.J. Kooi

Period: September 2009 – July 2010
Credits: 54 ECTS

Abstract

This thesis is devoted to the investigation of Casimir forces in phase-change materials (PCM's). Phase-change materials are compounds which become amorphous and crystalline under certain fast switchable conditions and moreover they show strong contrast in optical and conductive properties between the amorphous and the crystalline state. This work shows that the change in optical properties will also lead to a significant difference in Casimir forces between the amorphous and the crystaline state. The obtained theoretical calculations were compared with experimental results obtained by force measurements. Casimir forces were measured between a gold coated sphere and a PCM coated plate. Both the experimental and theoretical approach showed that at moderate surface separations ~100 nm the force contrast is about 20 %. The latter holds a promise to use PCM's to attain force control in nanosystems.

Table of content

1 Introduction.

1.1 Casimir force

The Casimir effect was predicted in 1948 by H.B.G. Casimir and represents the attraction between a pair of neutral, parallel and perfectly conducting plates placed in vacuum. The field must satisfy certain boundary conditions at the surfaces of the conducting plates, and these boundary conditions rule out some of the modes (oscillators) that would otherwise exist in unbounded space. Since the density of the electric field oscillation modes (virtual photons) are lower between plates than outside them, there is a net pressure pushing the plates together (Fig. 1). Though the Casimir effect is expected to exist for any type of quantum field, in most cases this phenomenon is considered for the electromagnetic field in view of the fact that this is the strongest fundamental interaction and it is the most likely to generate measurable effects.

An important characteristic of the Casimir effect is that it is a macroscopic quantum effect. At the nanoscale this force is quite small and is now hardly within the range of modern laboratory sphere-plate force measurements systems. However when we go to proper macro scale objects, this force can have also macroscopic effect [9]. One very interesting and demonstrative effect of Casimir force in nature is the gecko ability to walk across the ceiling on both hydrophobic and hydrophilic surfaces. Since ancient Greece times people tried to explain this phenomena. They considered that it may be due to interlocking, glue, suction, friction, static electricity, capillary forces or van der Waals adhesion. By now all these prediction mechanisms where rejected except the last one. In a gecko type surface the magnitude of a force is around 10 N per cm^2. This mean that if such type of materials can be synthesized, then, for instance, with the area of human palms which has around 20 squared cm it will be possible to hold the weight of 200 kilograms. Now one can think of many interesting possibilities to implement this force through artificial biomimetic systems: modern micro-grippers for a tissue and sells, revolutionary wall-climbing ATVs and robots, micro-electrical interconnects, novel pressure controlled dry adhesives for all air, liquid and vacuum environments. A nice feature of gecko adhesives is that they do not rely on

chemical bonds, they are nontoxic, nonirritating and glue free and one day they may be used in biomedical applications such as tissue and endoscopy adhesives, replace screws, glues and interlocking tabs in such applications as automobile dashboards or mobile phones.

Another main feature of the Casimir force is its strong dependence on shape, switching from attractive to repulsive as a function of the geometry and of the coupling with the constraining objects. This makes the Casimir force a strong candidate for applications in nano-technologies and micro- or nano-electromechanical devices.

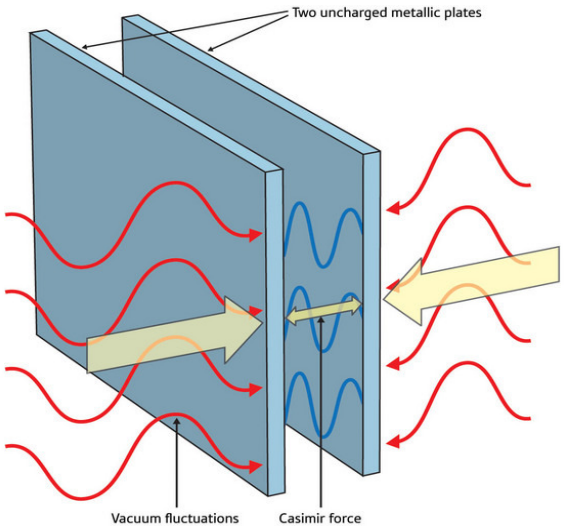

Figure 1: Two uncharged plates in a vacuum will experience an attractive force, which arises because the plates alter the fluctuations in the vacuum.

Finally, many novel theories have predicted the existence of large extra dimensions in unified field theories of the fundamental forces. These dimensions, according to them, could modify classical Newtonian gravitation at sub-millimeter distances. Measuring the Casimir effect very precisely, while at the same time performing precise theory calculations, could therefore help physicists to test the validity of such radical theories [11].

1.2 Historical perspective

It is known that interatomic van der Waal dispersive forces falls as the sixth power of the separation between the atoms. However, for instance with metallic materials, when one goes to the separations between them larger than approximately 10% of the plasma wavelength of these materials, then the force

appears to fall faster then $1/d^6$. Hendrik Casimir and Dik Polder started to solve this problem. They considered a system of a single atom in an electromagnetic cavity with perfectly conducting walls. Using the full zero temperature quantum electrodynamic treatment they calculated the atom's interaction with the cavity walls as a function of separation distance.

The simplicity of the final result inclined them to search for a fundamental explanation. After a talk with Niels Bohr, Casimir formulated a new approach and assigned a zero point energy to every mode in the cavity and obtained his famous result for the attractive force between two perfectly conducting plates at zero point temperature [4]:

$$F = -\frac{\pi^2 \hbar c}{240 d^4} \quad (1)$$

Therefore the Casimir force is the long range correction of van der Waals dispersive force taking into account the finite velocity of light. Casimir concluded his work in the set of three scientific papers. Since then these set of papers got thousand of citations and are considered one of the most important works done in physics, mostly because they show that boundary conditions of the system can affect the zero-point energy of a system and correspondingly its properties. In other words one can influence and manipulate with zero point energy of a system and to make use of it.

Later this work inspired Evgeny Lifshitz to generalize Casimir's electromagnetic mode boundary problem with perfectly conducting parallel plates at zero point temperature for real materials with some dielectric properties at any temperature. Then, a natural question is, can we somehow control the force by controlling the shape and dielectric properties of the materials? And this thesis is about the investigation of this question. Perfect candidates for such a material which has different states with different dielectric properties are phase change materials.

1.3 Phase-Change Materials

Phase-Change materials (PCMs) are materials which exist in at least two structurally distinct solid phases. The amorphous and crystalline phases can have very different optical and electrical properties. High contrast between the amorphous and the crystalline state, a switching time of a few tens of nanoseconds, and an operation cyclability up to 10^7 cycles makes them good candidates for various of applications if both phases are stable at an operating

temperature [8]. The transformation of the metastable amorphous phase to the energetically favorable, stable crystalline phase occurs by heating the material above its crystallization temperature for a time long enough for crystallization to occur. The reverse operation is performed by heating the crystalline material up to its liquid state and subsequently quenching it fast enough so that it solidifies in the amorphous state. PCM technology is already used commercially in memory storage applications. Figure 2 shows an example of amorphous to crystalline state transition of a blanket layer of phase change material, in this case doped fast growth SbTe material.

Phase-change materials change their properties even for sizes down to nanometers range. They loose their phase change properties for sizes only around 1-2 nm when not enough atoms are available to form the crystalline unit cell [32].

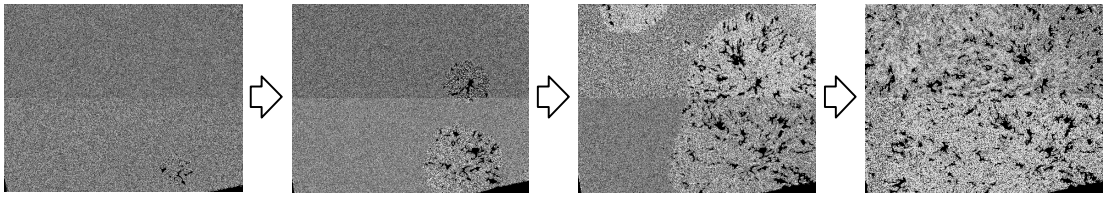

Figure 2: Doped SbTe fast growth material, as obtained by J. Oosthoek from Zernike Institute for Advanced Materials. Crystallization was performed at 170 ºC in the transmission electron microscope (TEM). The size of the sample is 2.9x2.3 μm.

Now there are also experiments where experimentalists are trying to go to superconducting state to get much higher contrast in dielectric properties between two states and to measure Casimir force difference in this case. But these experiments are not completed yet, and they are much more difficult.

1.4 Master Thesis Outline

Chapter 2 is about preparation and characterization of PCM's samples. This is done with ellipsometry, for which optical reflection analysis for multilayer systems is required. In Chapter 2 optical reflection theory is described, together with physical models for the optical response of a material. Chapter 3 describes a procedure of data analysis: extracting and extrapolating the dielectric response function from raw ellipsometry measurement data. Then extrapolation

was performed in ranges for which no dielectric measurement data was available. The applicability of these extrapolations is checked and analyzed by the generalized Kramers-Kronig consistency in Chapter 4. The obtained dielectric response allows Casimir force calculations for which the force depends on the dielectric function at imaginary frequencies. Calculations, comparison with the measurements and discussions of the Casimir force will be the topic of Chapter 5.

2 Optical response of materials.

2.1 Ellipsometry measurements

Ellipsometry is primarily used to determine optical properties (such as dielectric response function $\varepsilon = \varepsilon' + i\varepsilon''$) and thickness of thin films and to characterize composition, crystallinity, and doping concentration. It measures the change in polarization as light reflects or transmits from a material. The initial polarization of the light beam is known, then the beam is reflected or transmitted from the sample, and the output polarization is measured (Fig 3.). The polarization change ρ is represented as an amplitude ratio between r_p and r_s, the p-polarized and s-polarized complex Fresnel reflection coefficients:

$$\rho = \frac{r_p}{r_s} = \tan\Psi e^{i\Delta} \qquad (2)$$

Ψ and Δ are the raw data in a measurement as a function of wavelength λ.

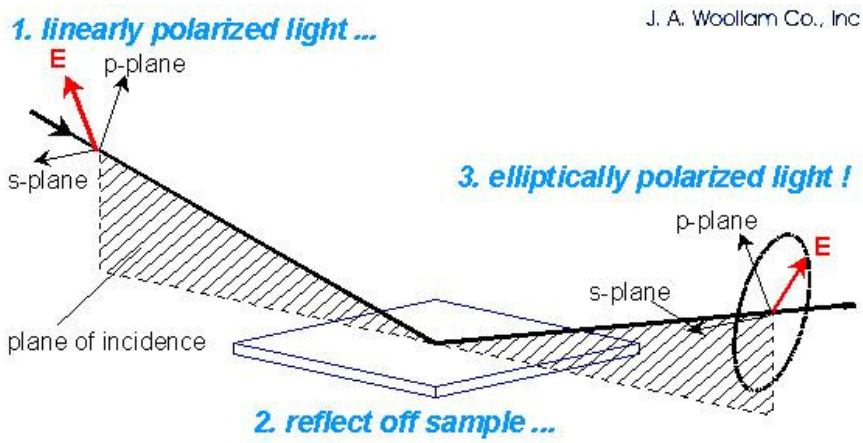

Figure 3: Schematic of the ellipsometry setup.

The main advantage of ellipsomenry over intensity based refraction is that the ellipsometry is not sensitive to changes in absolute intensity of measurement beam. For intensity measurements calibration and control of the beam intensity is very hard. When measuring polarization, the beam intensity is not an important measurement parameter. Reflection or transmission measurements only give one parameter (refractive index n or extinction coefficient k). However, ellipsometry measures two parameters {Ψ, Δ} at each wavelength, which gives more information compared to intensity reflection measurement and allows extracting both k and n. The phase information Δ allows investigations of even subnanometer thickness thin films.

A light source produces unpolarized light which is then sent through a rotating polarizer. Then the linearly polarized light reflects from the sample surface and passes through an analyzer. The analyzer determines the reflected polarization. This information is compared to the known input polarization to determine the polarization change caused by the sample reflection. This is how the ellipsometry measurement of Ψ and Δ is obtained.

Within the context of measuring Casimir forces for phase-change materials, we prepared 1 μm thick amorphous AgInSbTe (AIST) thin films onto standard Al coated Si wafers, of which half of the AIST films are annealed to the crystalline state. The roughness of these materials was a few nm rms. The optical data of crystalline and amorphous AIST films where obtained by J. A. Woollam Co., Inc. (USA). The vacuum ultraviolet variable angle spectroscopic ellipsometer covers the spectral region from 0.041 to 8.67 eV at two angles of incidence θ_1=60° and θ_2=75°. Measuring for two angles of incidence is used for controlling the measuring system. Ellipsometry measurement data should not

depend on θ. Indeed the obtained difference between θ_1=60° and θ_2=75° values of {Ψ, Δ} varies less then ~0.01 %.

In the case of bulk material, the equations derived for a single reflection can be directly inverted to obtain the dielectric function from the ellipsometry measurement, *r* [5]:

$$\varepsilon = \sin^2\theta\left[1+\tan^2\theta\left(\frac{1-\rho}{1+\rho}\right)^2\right] \qquad (3)$$

This equation assumes there are no surface layers of any type (surface oxide or roughness). If multilayers are present, the pure dielectric function should be extracted with the techniques described in the next section.

2.2 Light reflection on multilayers

In our case below the AIST film there was an aluminum layer deposited on a silicon surface. The dielectric function of aluminum ε is already known [1,2]. Instead of using ε a material is often characterized by the complex refractive index $N = n + ik = \sqrt{\varepsilon}$, where k is the extinction coefficient. The pure dielectric function of AIST can be extracted from ellipsometry raw data using the Fresnel equations [7]:

$$r_p = \frac{n_t\cos\theta_i - n_i\cos\theta_t}{n_t\cos\theta_i + n_i\cos\theta_t}, \qquad (4)$$

$$t_p = \frac{2n_i\cos\theta_i}{n_t\cos\theta_i + n_i\cos\theta_t}, \qquad (5)$$

$$r_s = \frac{n_i\cos\theta_i - n_t\cos\theta_t}{n_i\cos\theta_i + n_t\cos\theta_t}, \qquad (6)$$

$$t_s = \frac{2n_i\cos\theta_i}{n_i\cos\theta_i + n_t\cos\theta_t}, \qquad (7)$$

where θ_i, θ_t are respectively the incident and transmitted angle, and n_i, n_t are respectively the refractive indexes of incident and transmittance medium. $r_p \equiv \frac{E_{rp}}{E_{ip}}$, $t_p \equiv \frac{E_{tp}}{E_{ip}}$, $r_s \equiv \frac{E_{rs}}{E_{ip}}$, $t_s \equiv \frac{E_{ts}}{E_{is}}$ are the amplitude reflection and

transmission coefficients for the p- and s-polarization components respectively. Figure 4 shows the boundary of two materials where these equations apply.

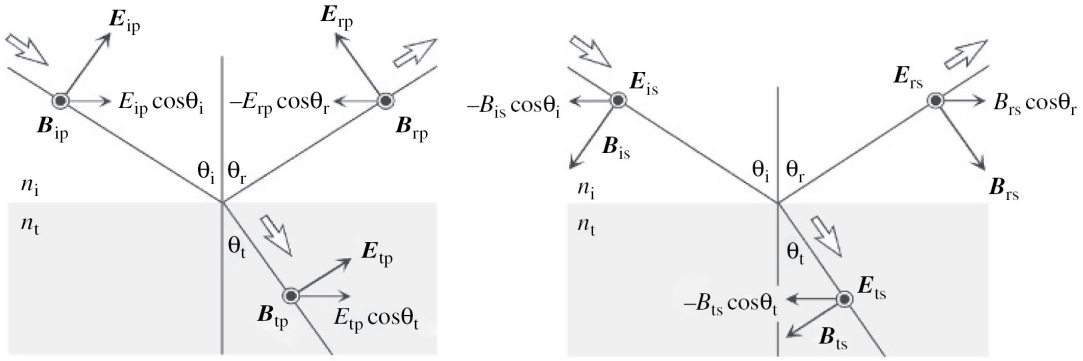

Figure 4: Electric field ***E*** and magnetic induction ***B*** for (a) p-polarization and (b) s-polarization. [7]

The previous equations (4)-(7) still hold if the refractive index n is replaced by the complex refraction index N and therefore to the complex dielectric function $\varepsilon = N^2$. Moreover, using Snell's law $N_i \sin\theta_i = N_t \sin\theta_t$ one can represent the angle of transmittance θ_t as a function of the angle of incidence $N_t \cos\theta_t = \sqrt{N_t^2 - N_i^2 \sin^2\theta_i} = \sqrt{(\varepsilon_t - \varepsilon_i \sin^2\theta_i)}$. Then the Fresnel equations can be written as:

$$r_p = \frac{\frac{\varepsilon_t}{\varepsilon_i}\cos\theta_i - \sqrt{\frac{\varepsilon_t}{\varepsilon_i} - \sin^2\theta_i}}{\frac{\varepsilon_t}{\varepsilon_i}\cos\theta_i + \sqrt{\frac{\varepsilon_t}{\varepsilon_i} - \sin^2\theta_i}} \quad (8)$$

$$r_s = \frac{\cos\theta_i - \sqrt{\frac{\varepsilon_t}{\varepsilon_i} - \sin^2\theta_i}}{\cos\theta_i + \sqrt{\frac{\varepsilon_t}{\varepsilon_i} - \sin^2\theta_i}} \quad (9)$$

From these two equations the raw ellipsometry data $\rho = r_p / r_s$ can be directly converted to the dielectric function $\varepsilon_t = \sin^2\theta_i \left[1 + \tan^2\theta_i \left((1-\rho)/(1+\rho)\right)^2\right]$ [5]. In any case, the obtained dielectric function should be considered as an effective value $\langle \varepsilon_t(\lambda) \rangle$ because the film may not be completely isotropic. The film was also exposed to air so it may contain absorbed layers of different origins. As a result the extracted dielectric function is an averaged quantity.

Now we consider a two-layer system (Fig. 5). The zero medium is air, the second and third are the AIST film and aluminum wafer respectively. Light reflects from the AIST surface but it also reflects from AIST-Aluminum interface. This multilayer effect is extremely important for the amorphous AIST film. However for the crystalline AIST, the reflection from the AIST-aluminum interface can be neglected because for metals light in our spectral range will not penetrate the film deep enough to cause a second reflection.

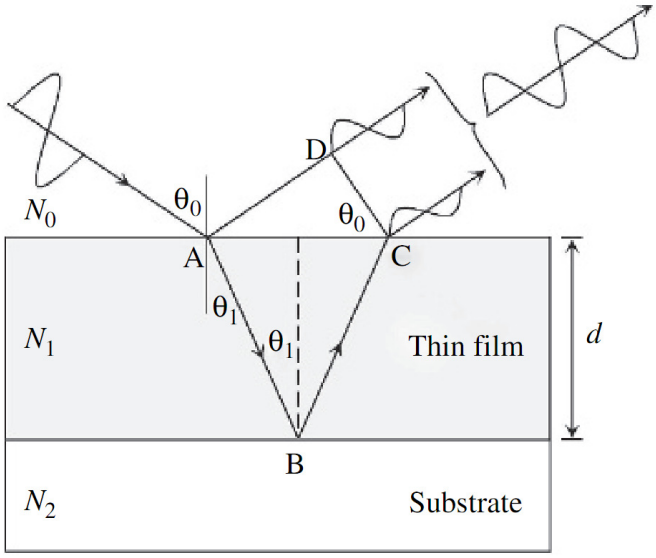

Figure 5: Optical interference in a thin film coated on a substrate [7]

The total phase difference between two beams can be calculated as follows:

$$\delta = \frac{2\pi N_1}{\lambda}(\overline{AB} + \overline{BC}) - \frac{2\pi N_1}{\lambda}\overline{AD} \qquad (10)$$

$$AD = AC\sin\theta_0 = 2d\sin\theta_0\tan\theta_1 = 2d\frac{N_1}{N_0}\frac{\sin^2\theta_1}{\cos\theta_1} \qquad (11)$$

$$AB = AC = \frac{d}{\cos\theta_1} \quad (12)$$

$$\delta = \frac{4\pi d}{\lambda}N_1\left(\frac{1}{\cos\theta_1} - \frac{\sin^2\theta_1}{\cos\theta_1}\right) = \frac{4\pi d}{\lambda}N_1\cos\theta_1 \quad (13)$$

The phase difference between the surface and the interface is

$$\beta = \frac{\delta}{2} = \frac{2\pi d}{\lambda}N_1\cos\theta_1 = \frac{2\pi d}{\lambda}\sqrt{N_1^2 - N_0^2\sin^2\theta_0} \qquad (14)$$

The figure 6 illustrates the optical interference in our system under consideration.

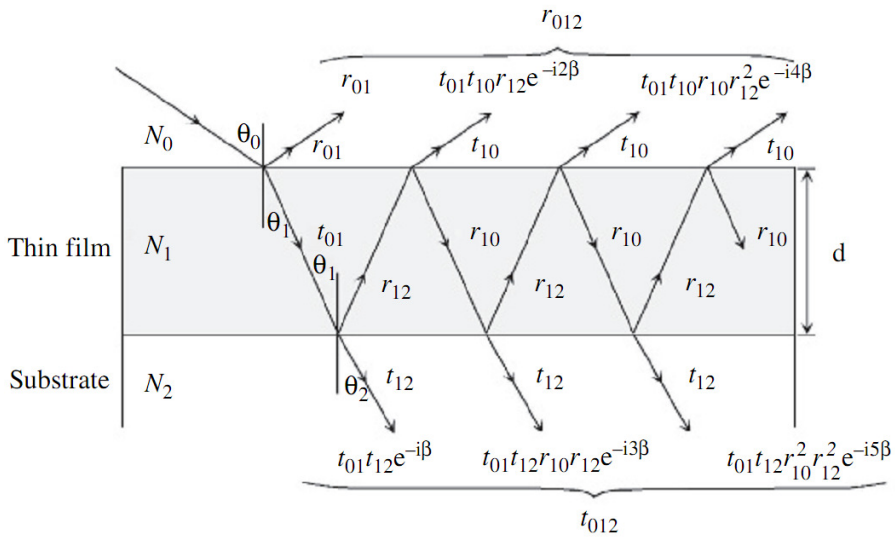

Figure 6: Optical model for an ambient/thin film/substrate structure [7]

The amplitude reflection coefficient for entire structure is expressed from the sum of all reflected waves:

$$r_{012} = r_{01} + t_{01}t_{10}r_{12}e^{-2i\beta} + t_{01}t_{10}r_{10}r_{12}^2e^{-4i\beta} + t_{01}t_{10}r_{10}^2r_{12}^3e^{-6i\beta} + \ldots \qquad (15)$$

r_{ij}, t_{ij} are the amplitude reflection and transmission coefficients between the mediums i and j, and $e^{-2i\beta}$ is the phase variation factor caused by the difference in optical pass length. One can see here the geometric progression and the final amplitude reflection after summation is:

$$r_{012} = r_{01} + \frac{t_{01}t_{10}r_{12}e^{-2i\beta}}{1 - r_{10}r_{12}e^{-2i\beta}} \qquad (16)$$

This can be simplified by using the relations $r_{10} = -r_{01}$, $t_{10}t_{01} + r_{01}^2 = 1$ which directly follow from the Fresnel equations.

$$r_{012} = \frac{r_{01} + r_{12}e^{-2i\beta}}{1 + r_{01}r_{12}e^{-2i\beta}} \qquad (17)$$

This formula is correct for both s- and p-polarized light. Finally for the raw ellipsometry data we obtain:

$$\rho = \frac{r_{012,p}}{r_{012,s}} = \frac{\dfrac{r_{01,p} + r_{12,p} e^{-2i\beta}}{1 + r_{01,p} r_{12,p} e^{-2i\beta}}}{\dfrac{r_{01,s} + r_{12,s} e^{-2i\beta}}{1 + r_{01,s} r_{12,s} e^{-2i\beta}}} \quad (18)$$

This equation holds for each single measured wavelength λ (or each single frequency ω). The reflection coefficients can be expressed via the angle of incidence and dielectric functions of the AIST film and aluminum substrate by using the formulas (16) and (17).

One can see that after the last substitution this equation contains only one unknown value, the dielectric function of AIST. The thickness of the AIST film, angle of incidence, and the dielectric function of aluminum is known. To be more correct the dielectric function of the aluminum substrate should have been measured in the analogous ellipsometry experiment. Every substrate has unique features because of different conditions of preparations. But data for our specific aluminum layers is lacking, therefore we will use tabulated data for aluminum. In fact, we need the values for the aluminum dielectric functions in the range of wavelengths as obtained with ellipsometry. The substrate material data where interpolated.

3 Data analysis

3.1 Results of the numerical simulations

For the crystalline AIST film light transmission is very low and second reflection from the aluminum wafer can be neglected. Equation (3) can be used to convert ellipsometry raw data to the dielectric response function directly [6]. And it is closely Kramers-Kronig-consistent (for the Kramers-Kronig-consistency see paragraph 4.1). The obtained data are shown in figure 7. However for the amorphous case taking into account the aluminum wafer is crucial, thus we use

equation 18. Extraction of pure data for the amorphous AIST sample is explained below.

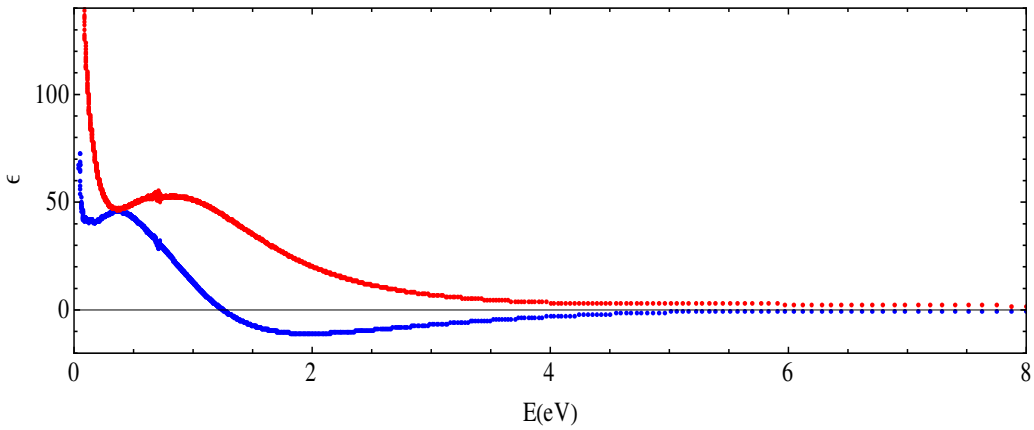

Figure 7: Obtained complex dielectric response function for the crystalline film. Red and blue points indicate the imaginary and real part of the dielectric response function respectively.

Equation (18) cannot be solved only numerically. Because of phase variation factor $e^{-2i\beta}$ which is periodical and contains the unknown ε_1 ($\beta = \frac{2\pi d}{\lambda}\sqrt{\varepsilon_1 - \sin^2\theta_0}$), equation (18) has infinite number of solutions. However, only one of them is Kramers-Kronig consistent and corresponds to the physical value of ε_1.

Usually for this kind of problems the equations are solved numerically when one specifies the starting point near which the solution should be found, and after performing a certain number of iterations one obtains a value of this specific solution. After enumerating all selected starting points in a defined interval one can obtain points-candidates for the true solution in this specific interval.

The dielectric response function for the aluminum wafer was taken from articles [1, 2], and then interpolated in the region of interest. The behavior of the complex refractive index for the aluminum is shown on figure 8.

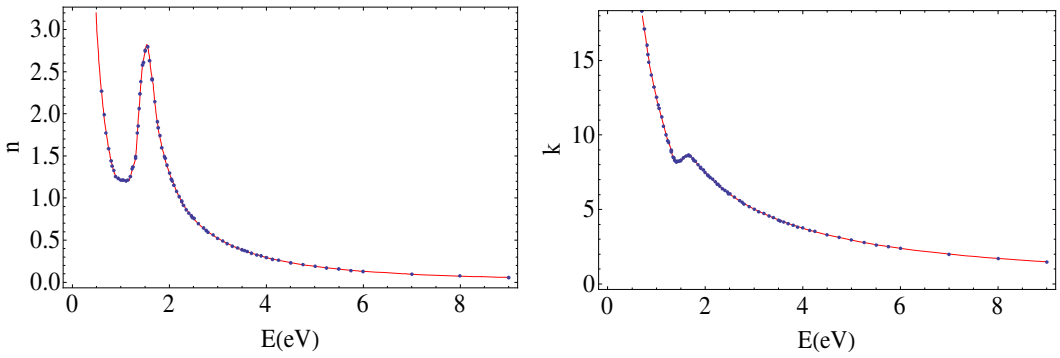

Figure 8: Complex refractive index $\tilde{n} = n + ik$ extrapolation for the aluminum wafer.

To separate the true solution a priori one can say that for the amorphous film the absorption term k is very low. Therefore n cannot vary significantly (Kramers-Kronig-consistency). Since n is about 4.5 in near IR range, it cannot vary significantly from this value in the far IR. Therefore, when the frequency tends to zero the reflection coefficient n should converge to some finite value closely to n≈4.5. For both crystalline and amorphous films when the frequency goes to infinity ω→∞, n should converge to one and k should converge to zero; (n, k) → (1, 0). This can be explained according to the free electron Lorentz model (for more detail see sec. 3.2). At high enough frequencies the electrical dipoles of the material are not able to follow the orientation of the incoming field and they are not able to quench it. However, in the case of the crystalline film and for the low frequencies (according to the Drude model) electrons under the influence of the incoming external field are able to redistribute to compensate the force inside the material completely. As a result n tends to infinity; $n \to \infty$.

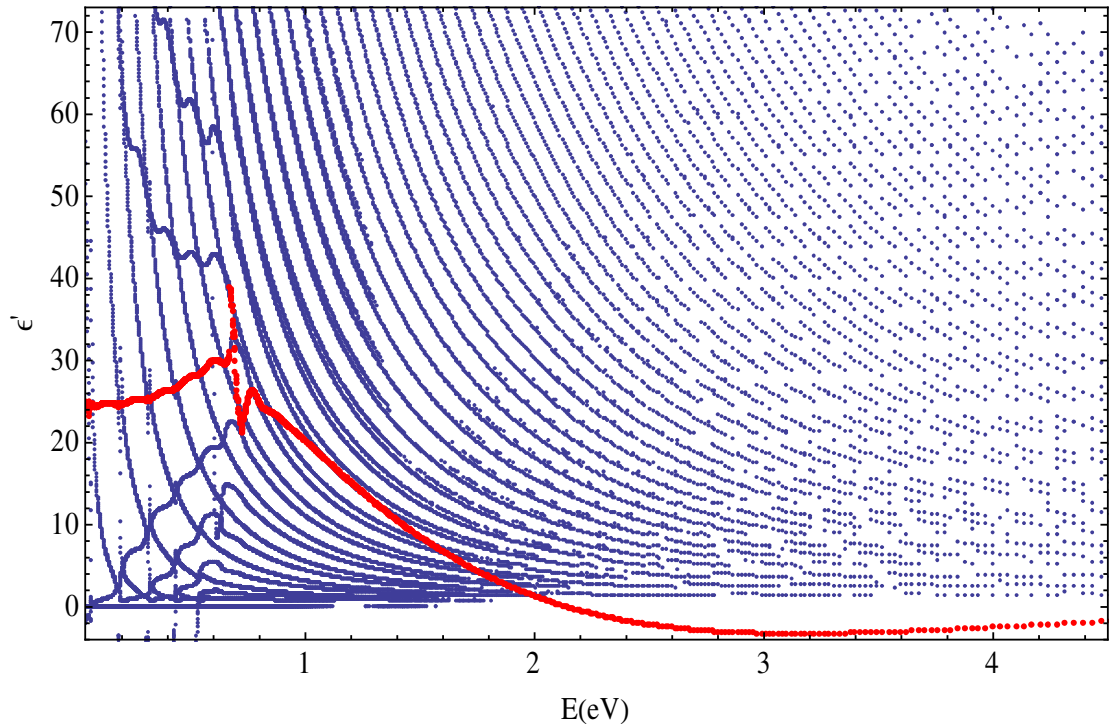

Figure 9: Obtained set of the solutions for the real part of the dielectric response function. Red points indicate selected true, KK-consistent solution.

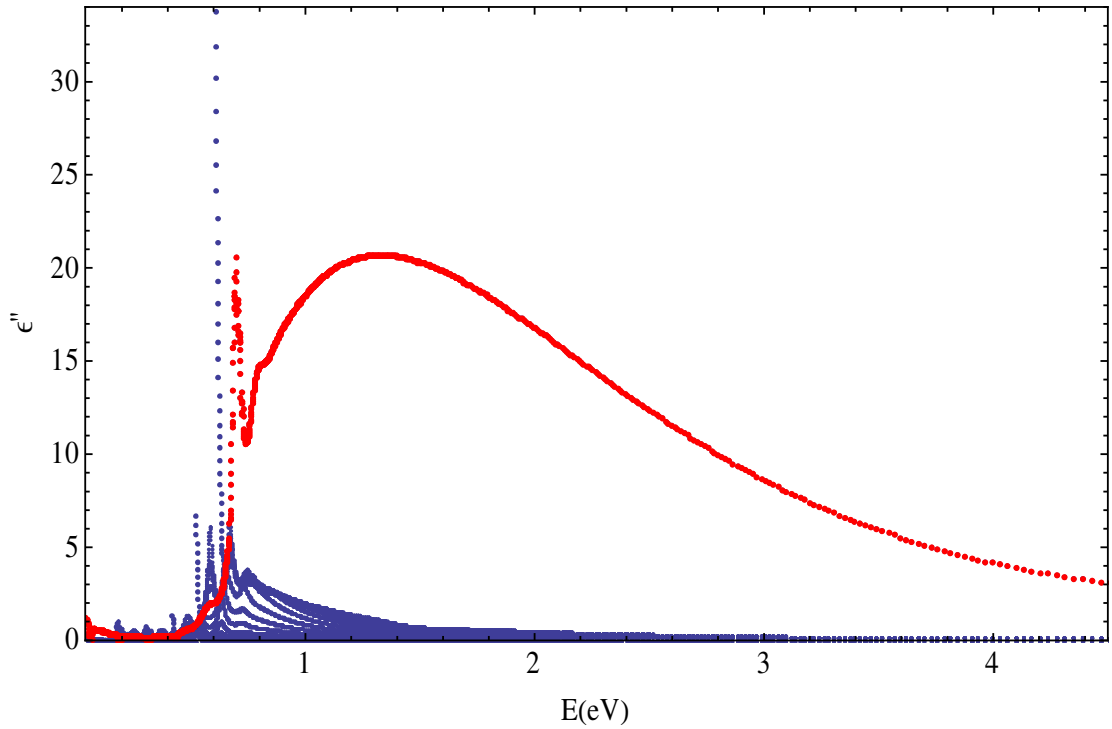

Figure 10: Obtained set of the solutions for the imaginary part of the dielectric response function. Red points indicate selected true, KK-consistent solution.

The analysis allowed to distinguish the different sets of the solutions (see Figures 9,10). The problem was that some families of the curves intercept, and it is not obvious which part of the curve (starting from one interception and finishing on another) corresponds to which solution. If we start from the very first point in the UV region and one by one point try to separate a distinct solution by selecting the next nearest points we will get complications in these interception regions. Luckily these regions are rare. One of them is shown in figure 11 in the 0.6-0.85 eV energy range where strong dispersion starts.

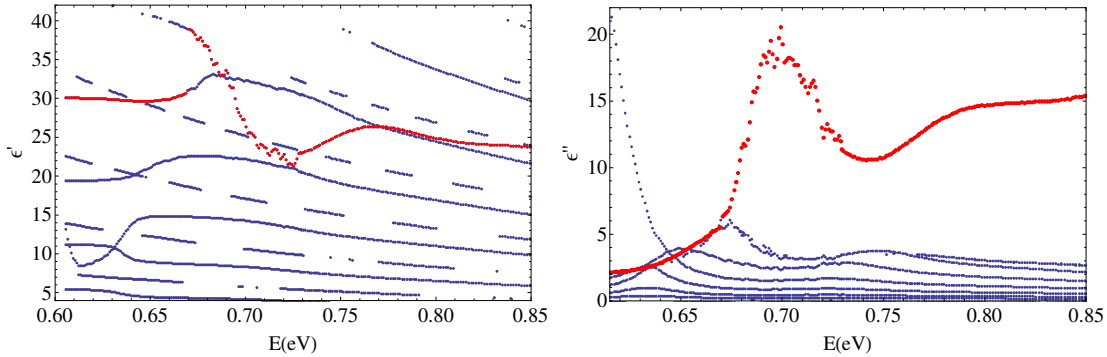

Figure 11: Dielectric response function set of the solutions in the near IR range.

Another problem was that we have only 1345 frequencies (data points) and this number does not allow us to obtain all the families of solutions clearly enough. From figure 12 for the UV energy range one can see that some curves are complete enough, while others consist of some parts only. One of the possibilities to clarify these solutions is to continuously extrapolate 1345 available data points to be able to investigate these specific regions. But one can see that it is not necessary for the final purpose because one solution has quite unique behavior. This curve is absolutely distinct from the others in the range from near IR to visible, especially the imaginary part of the dielectric response function (Fig 12). Later it will be shown that this curve is indeed Kramers-Kronig-consistent. However in the far IR range the situation is more complex (Figure 13). The various multiple down-peaks is something that does not reproduce the true imaginary part of the dielectric response function ε'' in the far IR range. Sometimes ε'' even goes to negative values which can never hold in real physical systems. These peaks are present because ellipsometry cannot distinguish between Δ and $\Delta+180°$ for the raw measurement data.

$$\rho = \frac{r_p}{r_s} = \tan\Psi e^{i\Delta} \qquad (19)$$

As was explained above a priori we expect that refractive index n for the amorphous AIST should not vary much from the value 4.5 in the IR range and this reduces a lot of candidates for the true solution.

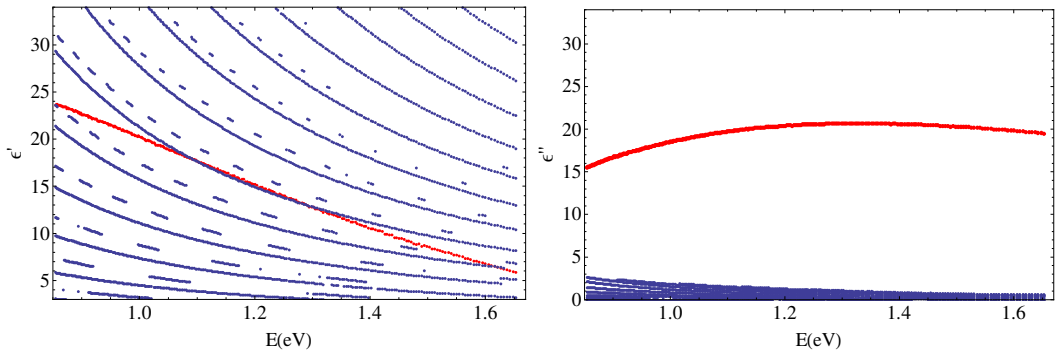

Figure 12: Dielectric response function set of the solutions from near IR to visible range.

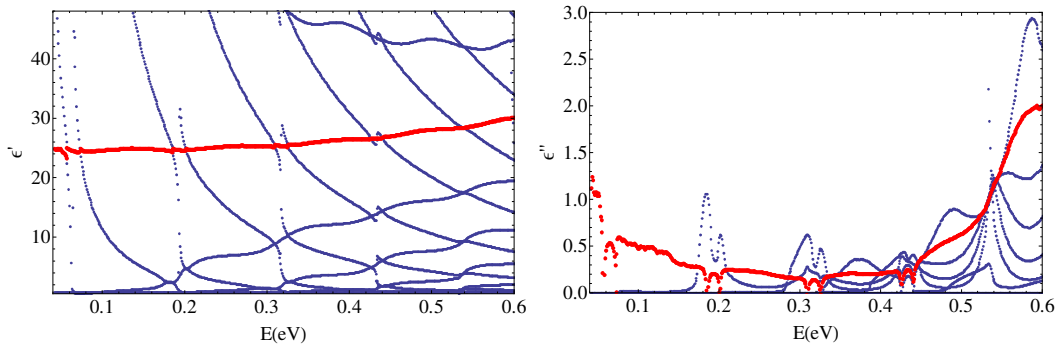

Figure 13: Dielectric response function set of the solutions in the far IR range.

After accurate selection of different part curves combinations in the visible and IR energy range the true solution was defined (Fig 14). In the UV range it is the one that was mentioned before with quite distinct behavior.

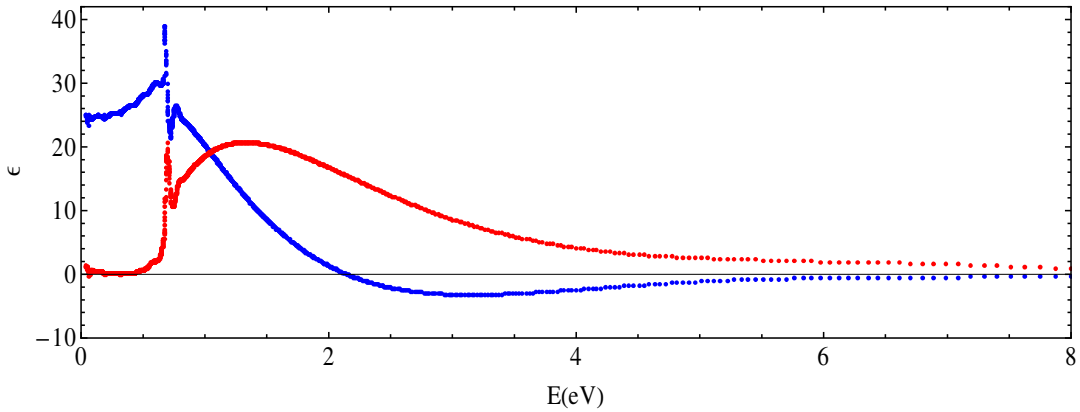

Figure 14: Obtained complex dielectric response function for the amorphous film. Red and blue points indicate imaginary and real part of the dielectric response function respectively.

3.2 Drude IR and Lorentz UV extrapolation

At low frequencies experimental data are not accessible. The low frequency cut-off (0.4 eV in our data) is especially important in the case of crystalline AIST. This data can be extrapolated using the Drude free electron model, the classical description of electron motion in metals, [5]

$$\varepsilon(\omega) = 1 - \frac{\omega_p^2}{\omega(\omega + i\omega_\tau)}. \qquad (20)$$

This equation contains two parameters. ω_p is the plasma frequency, and ω_τ is the relaxation frequency. The plasma frequency is defined by

$$\omega_p = \sqrt{\frac{n_e e^2}{\varepsilon_0 m_e^*}} \qquad (21)$$

where n_e is the number of electrons per unit volume, m_e^* is the effective mass of the electron, e - is the charge. m_e^* and n_e are in general unknown. The plasma and relaxation frequency are the fitting values and they was defined by fitting IR dielectric response range with Drude free electron model. Let us for instance consider an imaginary part of dielectric response function $\varepsilon''(\omega) = \omega_p^2 \omega_\tau / \omega(\omega^2 + \omega_\tau^2)$. In the IR range $\omega << \omega_\tau$, so that we obtain

$\varepsilon''(\omega) \propto \omega_p^2 / \omega\omega_\tau$. The latter means that as long as ω_p^2 / ω_τ remains the same ω_p and ω_τ can vary drastically. This explains why the obtained ω_p and ω_τ vary so much by changing the fitting parameters, such as the number of fitting points. However, precise calculation of ω_p and ω_τ is outside the scope of this Master thesis work. After obtaining ω_p and ω_τ the dielectric response function was extrapolated below the low-frequency cut-off. For fitting the real part of crystalline data, the factor 1 in the right hand side of eq. (20) has to be replaced by a fitting parameter representing core-electron contributions.

For the amorphous film $\varepsilon''(x)$ below the low-frequency cut-off is considered to be equal to zero. Above the high frequency cut-off (8.6 eV) we extrapolated by using the Lorentz oscillator model [22]. This is a purely classical model. Lorentz thought of an atom as a mass connected to another smaller mass (the electron) by a spring [22]. The spring is sent into motion by an electric field interacting with the charge of the electron:

$$\ddot{x}(t) + 2\gamma\dot{x}(t) + \omega_o^2 x(t) = \frac{e}{m_e} E(t) \qquad (22)$$

with $E(t)$ the electrical field , γ the damping rate and $m\omega_o^2$ the restoring force of the spring. The linear restoring force is just the dipole approximation of electron-atom interaction. The Lorentz model is often used for resonant absorptive processes. The dielectric response function in the oscillator model is given by:

$$\varepsilon(E) \propto \frac{1}{E_o^2 - E^2 - iEE_\gamma} \qquad (23)$$

where E_γ and E_0 are the fitting parameters, and they are respectively the broadening and the center energy.

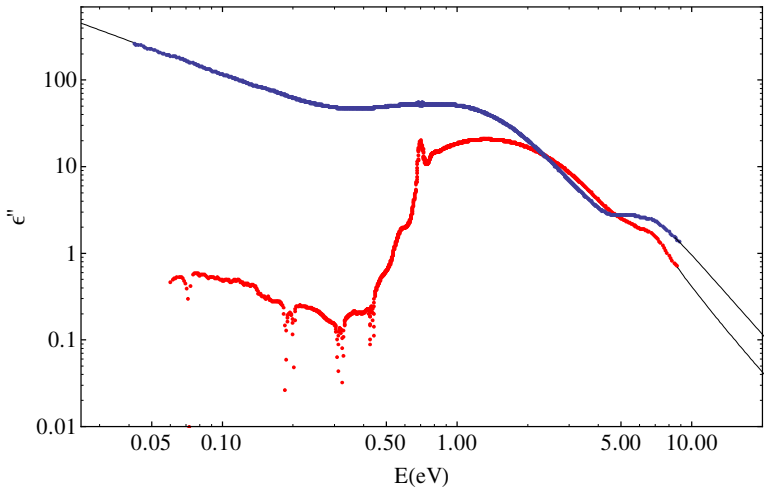

Figure 15: Dielectric response function for the amorphous and crystalline films with the Drude and Lorentz extrapolation in loglog scale.

4 Generalized Kramers-Kronig consistency.

4.1 Canonical Kramers-Kronig-consistency

The dielectric response function or the relative permittivity $\varepsilon(\omega)=\varepsilon'(\omega)+i\varepsilon''(\omega)$ is an analytic complex function in the upper half plane. Analyticity of this function implies casuality of our physical system. This means that the true solution must be the only one that is Kramers-Kronig consistent (KK-consistent). After separating the distinct solution one has to check the real and imaginary parts for KK-consistency. These relations where first derived by Ralph Kronig and Hendrik Anthony Kramers. First we consider a closed contour integral in the form:

$$\oint \frac{u(\omega')}{\omega'-\omega} d\omega' \quad (24)$$

Where $u(\omega')$ is an analytic function in the upper half plane and $u(\omega') \to 0$ as $\omega' \to \infty$. The contour consist of the upper half plane part extending to infinity, a small hump over the pole at $\omega = \omega'$ and part along the real axis (fig. 16).

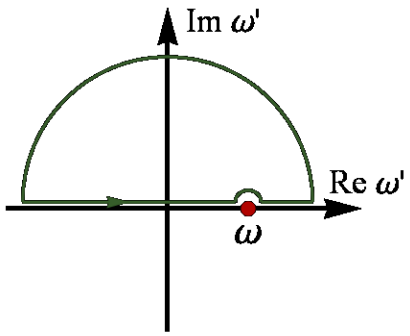

Figure 16: Closed loop integral over function $u(\omega')/\omega'-\omega$ in complex plane in order to derive relation between real and imaginary part of $u(\omega')$.

The part at the infinity vanishes and a half circle part around the point $\omega = \omega'$ residue theorem are equal to $-i\pi u(\omega')$. This implies:

$$\oint \frac{u(\omega')}{\omega'-\omega} d\omega' = P\int_{-\infty}^{\infty} \frac{u(\omega')}{\omega'-\omega} d\omega' - i\pi u(\omega') = 0 \quad (25)$$

where P is the Cauchy principal value. Thus,

$$u(\omega) = \frac{1}{i\pi} \int_{-\infty}^{\infty} \frac{u(\omega')}{\omega'-\omega} d\omega' \quad (26)$$

By taking the real and imaginary part of the previous expression one can obtain the following expressions:

$$\mathrm{Re}[u(\omega)] = \frac{1}{\pi} \int_{-\infty}^{\infty} \frac{\mathrm{Im}[u(\omega')]}{\omega'-\omega} d\omega' \qquad (27)$$

$$\mathrm{Im}[u(\omega)] = -\frac{1}{\pi} \int_{-\infty}^{\infty} \frac{\mathrm{Re}[u(\omega')]}{\omega'-\omega} d\omega' \qquad (28)$$

An important fact is that the imaginary and real parts are interconnected and it is possible to obtain the complete complex function given only by one of its parts. One important thing to mention here is that this kind of relations appears in a kind of problems which involve response function of the system to an external applied force. For example, when an external electric field can induce the dipole moment of an atom.
Now, we suppose that the function satisfies the next symmetry relation:

$$u(-\omega) = u^*(\omega) \quad (29)$$

Which means that the real part is an even function and the imaginary part is an odd function. This type of symmetry exists in dielectric response functions of real materials. Let us also denote for simplicity its complex and real part shortly by $u''(\omega)$, $u'(\omega)$ respectively, so that $u(\omega) = u'(\omega) + iu''(\omega)$. If one multiplies both numerator and denominator by $\omega' + \omega$, then one can expand this expression into two parts.

$$u'(\omega) = \frac{1}{\pi} P \int_{-\infty}^{\infty} \frac{\omega' u''(\omega')}{\omega'^2 - \omega^2} d\omega' + \frac{\omega}{\pi} P \int_{-\infty}^{\infty} \frac{u''(\omega')}{\omega'^2 - \omega^2} d\omega' \quad (30)$$

The second part of eq. (30) will vanish due to the fact that $u''(\omega)$ is odd, and integration interval of the first part can be changed because of the even nature of $u'(\omega)$:

$$u'(\omega) = \frac{2}{\pi} P \int_{0}^{\infty} \frac{\omega' u''(\omega')}{\omega'^2 - \omega^2} d\omega' \quad (31)$$

Analogously with the formula (31) one can obtain:

$$u''(\omega) = -\frac{2}{\pi} P \int_{0}^{\infty} \frac{\omega u'(\omega')}{\omega'^2 - \omega^2} d\omega' = -\frac{2\omega}{\pi} P \int_{0}^{\infty} \frac{u'(\omega')}{\omega'^2 - \omega^2} d\omega' \quad (32)$$

These are alternative forms of Kramers-Kronig relations for the case where data exists only in region $\omega > 0$. Analogously, using symmetry relations for the dielectric function one can derive the Kramers-Kronig relations for this function:

$$\varepsilon'(\omega) = 1 + \frac{2}{\pi} P \int_0^{\infty} \frac{x\varepsilon''(x)}{x^2 - \omega^2} dx \qquad (33)$$

The calculated KK-consistency for the selected complex refractive index solution of the amorphous sample is shown on a log-log scale in figure 17. There is a difference between the real part $\varepsilon'(\omega)$ of the relative permittivity and the value which was obtained from the imaginary part of relative permittivity via eq. (33) in the far IR range. However, the last curve has all the unique features of the first one. Better KK-consistency can be achieved if experimental data beyond 8.6 eV is known. This is because there might be some other resonant peaks above this high frequency cut-off range which we cannot account for yet. Note that the Lorentz oscillator model extrapolation does not take them into account.

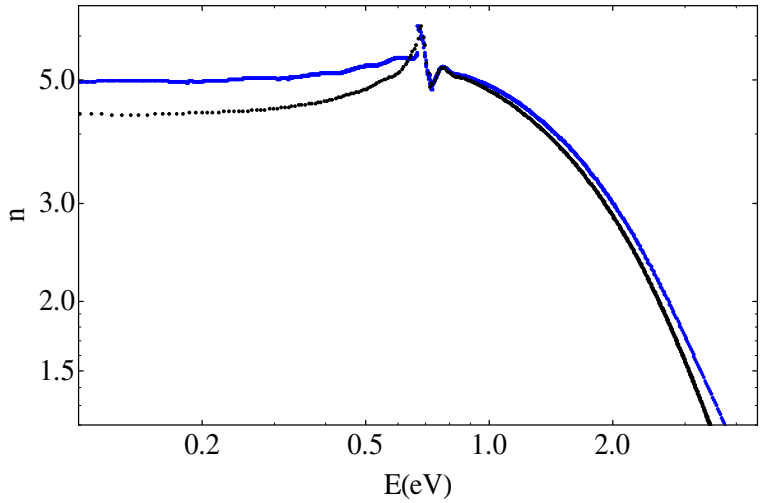

Figure 17: Kramers-Kronig consistency for the selected complex refractive index solution of the amorphous sample. The blue curve indicates the real part of the complex refractive index, and the black curve indicates that obtained using KK- consistency via the imaginary part of the complex refractive index.

Here we are interested only in $\varepsilon''(x)$ because if we know this we can find the relative permittivity at imaginary frequencies $\varepsilon(i\varsigma)$ which is not a physical value and it cannot be measured. Nevertheless, it contributes to the Casimir force since it is used for the force calculation in terms of the Lifshitz theory.

4.2 Window function method:

The Drude and Lorentz extrapolations which were used for our data give an error in the force calculation less than 1%. This is much less than the errors of the experimental measurements which are 7% for both the amorphous and crystalline AIST films. Therefore, further improvements of theoretical calculations are unnecessary. However the question *"Is it possible to avoid extrapolations?"* has its own scientific interest. In a resent article Giuseppe Bimonte described a method of modified Kramers-Kronig consistency [34]. By introducing an additional multiplier, the so called window function, to a dielectric response function, integrations over frequency can be done in a finite range from $\omega_{\min}$ to $\omega_{\max}$. This can be achieved due to the fact that the introduced window function changes the weight of contribution of different frequencies. With a proper chosen window function frequencies outside the ellipsometry measurement range will contribute to the overall integral much less and can be omitted. Bimonte's article shows application of this method using an idealized dielectric response function model for gold which is considered to be perfectly Kramers-Kronig consistent. However real measurements data has always some degree of inconsistency and this paragraph describes implementation of this window function method for such real data. Calculations of the effect on the dielectric response function at imaginary frequencies, and the effect on a Casimir force of this method were performed for amorphous, crystalline, and gold data. Calculations with the gold data are the most demonstrative, and are shown therefore in details in the following paragraphs.

First, we will describe the method of Bimonte's generalized Kramers-Kronig consistency relation. First we consider a window function $f(z)$ which is analytic in the upper half complex plane without any poles, and we assume that it satisfies the following symmetry condition [34]:

$$f(-z^*) = f(z) \quad (34)$$

Now we consider equation (31) for $u(z) = f(z)(\varepsilon(z) - 1)$ which still satisfies all the properties required for this equation. Then for each ξ that $f(i\xi) \neq 0$, one can obtain the next generalized dispersion relation:

$$\varepsilon(i\xi) - 1 = \frac{2}{\pi f(i\pi)} \int_0^\infty \frac{\omega}{\omega^2 + \xi^2} \mathrm{Im}[f(\omega)(\varepsilon(\omega) - 1)] d\omega \quad (35)$$

The first trivial and obvious choices for the window function $f(z)$ are $f(z)=1$ and $f(z)=iz$. The first one is simply a reduction to a canonical dispersion relation. The second choice is one that is often used in dispersion relations for conductors or superconductors.

$$\varepsilon(\omega)=1+\frac{4\pi i}{\omega}\sigma(\omega) \quad (36)$$

$$\varepsilon(i\xi)-1=\frac{8}{\xi}\int_0^{\infty}\frac{\omega}{\omega^2+\xi^2}\mathrm{Im}[\sigma(\omega)]d\omega \quad (37)$$

Using the freedom of choosing the form of a window function and by adjusting its parameters we can diminish the unwanted contribution of inaccessible low and high frequency intervals. The natural choice of such form is the one where the window function goes to zero fast enough for both $\omega\to 0$ and $\omega\to\infty$ suppressing the contribution of these two regions. A convenient family of window functions is:

$$f(z)=z^{2p+1}\left[\frac{1}{(z-\nu)^{2q+1}}+\frac{1}{(z+\nu^*)^{2q+1}}\right] \quad (38)$$

Where ν is an arbitrary complex number with $\mathrm{Im}(\nu)<0$, and p and q are integers with $p<q$. For this form of window function one can see that for the limit $z\to 0$ these functions converges to zero like z^{2p+1}, and for $z\to\infty$ we have $f(z)$ to vanish like $z^{2(p-q)}$. Therefore, suppression of both the low and the high frequencies can be achieved. In this work the next two sets of parameters were considered: ($p=1, q=2$) and ($p=1, q=3$). For both cases the value of the arbitrary complex number is $\nu=(1-2i)\frac{eV}{\hbar}$.

The best way to investigate the implementation of this window function method is to expand integration over frequencies into three intervals:

$$\varepsilon(i\xi)-1=\frac{2}{\pi}\int_0^{\infty}\frac{\omega\varepsilon''(\omega)}{\omega^2+\xi^2}d\omega=I_{low}(\xi)+I_{mid}(\xi)+I_{high}(\xi) \quad (39)$$

where

$$I_{low}(\xi)=\frac{2}{\pi}\int_0^{\omega_{\min}}\frac{\omega\varepsilon''(\omega)}{\omega^2+\xi^2}d\omega \quad (40)$$

$$I_{mid}(\xi)=\frac{2}{\pi}\int_{\omega_{\min}}^{\omega_{\max}}\frac{\omega\varepsilon''(\omega)}{\omega^2+\xi^2}d\omega \quad (41)$$

$$I_{high}(\xi)=\frac{2}{\pi}\int_{\omega_{\max}}^{\infty}\frac{\omega\varepsilon''(\omega)}{\omega^2+\xi^2}d\omega \quad (42)$$

In this representation the main goal is to make $I_{low}(\xi)$, $I_{high}(\xi)$ as low as possible, so $I_{mid}(\xi)$ will be the more dominating part of integration and extrapolation will have less effect on Casimir force calculations. Figure 18 (left) shows the contribution weight of all three terms to the overall integral $\varepsilon(i\xi)-1=I_{low}(\xi)+I_{mid}(\xi)+I_{high}(\xi)$ for the trivial case $f(z)=1$ i. e. without applying the window function method in a range from 1 to 200 Matsubara terms. It can bee seen that low frequency term $I_{low}(\xi)$ prevail at low Matsubara terms and by increasing m start to contribute less and less. However, the high frequency term $I_{high}(\xi)$ increases by increasing m, and plays a more and more crucial role. This plot demonstrates how important the extrapolation is and how much the experimentally inaccessible frequencies contribute to the calculation of the dielectric response function at imaginary frequencies.

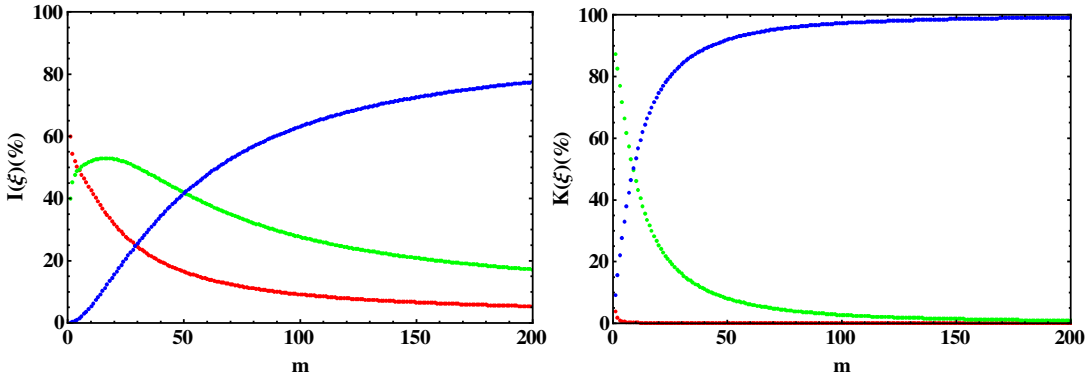

Figure 18: Contributions of different frequency range integrals to the overall result $\varepsilon(i\xi)-1$ for the trivial window function $f(z)=1$ are shown in percentage on the left plot. Red, green and blue data sets stand for $I_{low}(\xi)$ $I_{mid}(\xi)$ and $I_{high}(\xi)$ respectively. Plot to the right shows analogous results for the $f(z)=iz$. Matsubara ξ_m range is from 1 to 200.

Analogously, one can also show how the situation will change when one uses the $f(z)=iz$ window function. In this case formula (35) can be similarly expanded into three terms

$$\varepsilon(i\xi)-1=\frac{8}{\pi}\int_0^{\infty}\frac{\omega\,\mathrm{Im}[\sigma(\omega)]}{\omega^2+\xi^2}d\omega=K_{low}(\xi)+K_{mid}(\xi)+K_{high}(\xi) \quad (43)$$

Contributions to $\varepsilon(i\xi)-1$ of all three terms are shown in figure 18 (right). Although, now the role of the low frequency term $K_{low}(\xi)$ is drastically diminished and it is less then 0.5% starting from 4th Matsubara term, the contribution of $K_{high}(\xi)$ is more than in the previous case.

Finally we now can express how the situation will change if one uses the generalized Kramers-Kronig relation with window function given by (38):

$$\varepsilon(i\xi)-1=\frac{2}{\pi f(i\xi)}\int_0^{\infty}\frac{\omega}{\omega^2+\xi^2}\mathrm{Im}[f(\omega)(\varepsilon(\omega)-1)]d\omega=J_{low}^{(p,q)}+J_{mid}^{(p,q)}(\xi)+J_{high}^{(p,q)}(\xi)\,, \quad (44)$$

where

$$J_{low}^{(p,q)}(\xi)=\frac{2}{\pi f(i\xi)}\int_0^{\omega_{\min}}\frac{\omega}{\omega^2+\xi^2}\mathrm{Im}[f(\omega)(\varepsilon(\omega)-1)]d\omega \quad (45)$$

$$J_{mid}^{(p,q)}(\xi)=\frac{2}{\pi f(i\xi)}\int_{\omega_{\min}}^{\omega_{\max}}\frac{\omega}{\omega^2+\xi^2}\mathrm{Im}[f(\omega)(\varepsilon(\omega)-1)]d\omega \quad (46)$$

$$J_{high}^{(p,q)}(\xi)=\frac{2}{\pi f(i\xi)}\int_{\omega_{\max}}^{\infty}\frac{\omega}{\omega^2+\xi^2}\mathrm{Im}[f(\omega)(\varepsilon(\omega)-1)]d\omega \quad (47)$$

It can be seen from figure 19 (left and right) that the contribution of $J_{low}^{(p,q)}(\xi)$, $J_{mid}^{(p,q)}(\xi)$ again is almost fully diminished. The situation with the ($p=1, q=2$) and ($p=1, q=3$) parameter sets is much more improved. In the second parameters set ($p=1, q=3$) the high frequency term $J_{high}^{(p,q)}(\xi)$ is now less then 20% of the overall integral. However, the situation with the first set of parameters ($p=1, q=2$) is not so good. It can be seen clearly from both figures that starting from approximately the 60th Matsubara term, the $J_{high}^{(p,q)}(\xi)$ contribution start to diverge very fast, so this method can be implemented only for a number of Matsubara terms less then 60.

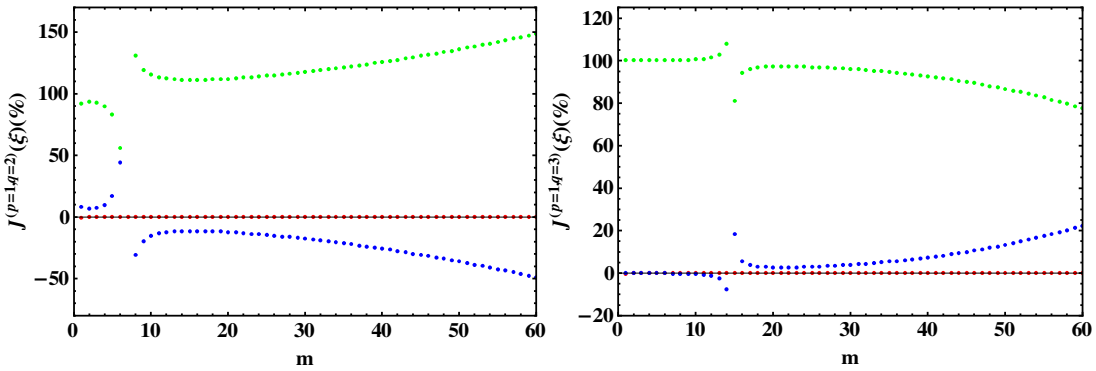

Figure 19: Contributions of different frequency range integrals to overall result $\varepsilon(i\xi)-1$ for the Bimonte's window function (eq. 38) with $(p=1, q=2)$ parameters set. The result is shown in percentage at the left plot. Red, green and blue data points sets stand for $J_{low}^{(p,q)}(\xi)$ and $J_{high}^{(p,q)}(\xi)$ respectively. Plot to the right shows the analogous results for the $(p=1, q=3)$ parameters set.

5 Casimir force

5.1 Lifshitz's theory for a sphere and a plate:

The force can be attractive or repulsive, depending on the specific arrangement of the materials and on their optical properties. Experimentally it is very hard to maintain the arrangement of perfectly parallel plates at nanometer separations, so the system of sphere and a plate is usually considered. Let us denote the sphere, plate and medium between them by 1, 2 and 3 respectively. Then according to Lifshitz's theory the Casimir force between a sphere and a plate is given by [3]:

$$F(l)=k_b TR\sum_{m=0}^{\infty}{}'\int_{k=0}^{\infty}k[\ln(1-r_{3,1}^{TE}r_{3,2}^{TE}e^{-2k_3 l})+\ln(1-r_{3,1}^{TM}r_{3,2}^{TM}e^{-2k_3 l})]dk \quad (48)$$

This formula accommodates temporal fluctuations of the field summing the individual oscillator free energies over an allowed set of frequencies. k_b and c are the fundamental physical constants of Boltzmann and speed of light, respectively. Summation at the $m=0$ term has half weight. This is called the

zero frequency term. $r_{3,i}^{TE}, r_{3,i}^{TM}$ are the reflection amplitudes with transverse-electric (s-polarization) and transverse-magnetic (p-polarization) respectively, and are given by

$$r_{3,i}^{TE} = \frac{k_i - k_3}{k_i + k_3} \quad (49)$$

$$r_{3,i}^{TM} = \frac{k_i \varepsilon_3 - k_3 \varepsilon_i}{k_i \varepsilon_3 + k_3 \varepsilon_i} \quad (50)$$

where k_i are the normal components of the wave vector in medium i

$$k_i = \sqrt{k^2 + \frac{\varepsilon_i \omega_m^2}{c^2}} \quad (51)$$

ε_1, ε_2 and ε_3 are the dielectric functions of the sphere, plate and intervening medium, respectively, evaluated on the set of imaginary Matsubara frequencies $\omega_m = \frac{2\pi k_b T}{\hbar} m$ according to the KK-transform [5]:

$$\varepsilon_i(i\varsigma) = 1 + \frac{2}{\pi}\int_0^\infty \frac{\omega \varepsilon_i''(\omega)}{\omega^2 + \varsigma^2} d\omega \quad (52)$$

In case of a gold and crystalline AIST film ε_1 and ε_2 respectively tend to infinity at zero frequency. Therefore, the TE- and TM-polarization reflection coefficients tend to $r^{TE} = 0$ and $r^{TM} = -1$.

5.2 Force calculations

Calculation of the force is very straightforward but some features should be mentioned. The zero term is not crucial for small separations of the order of 20 nm, but at a separation larger then 400 nm it starts to prevail among all other terms together. Formula (17) has the summation over an infinite number of Matsubara frequencies. However, 300 terms at separation distances from 10 to 500 nm gives an error less then 0.1%. A higher separation distance leads to

faster convergence and consequently less summation terms needed. Adding more terms to get higher accuracy is not necessary because the error of the experimental Casimir force measurements is about 7% for the system under investigation.

Figure 20 shows the results of the force calculations. The Casimir force decreases in magnitude of approximately ~20 % when the transition from the crystalline to amorphous state takes place. Therefore, 2 orders of magnitude decrease in dielectric properties, results in only 20% difference in force.

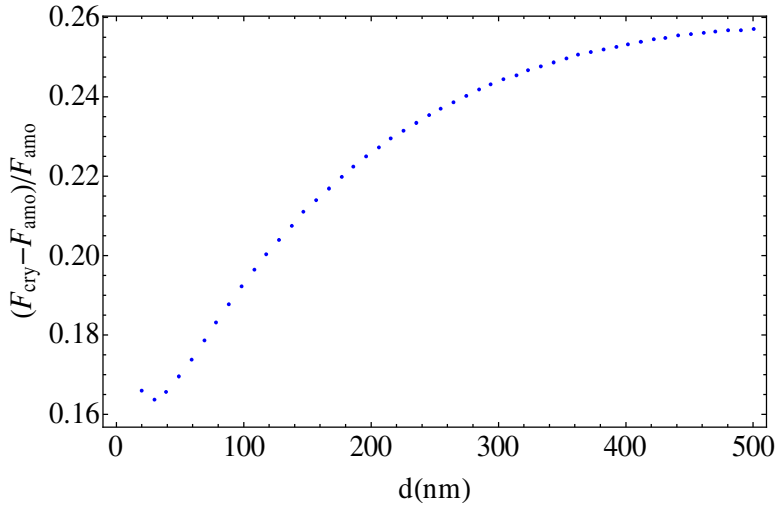

Figure 20: Calculated dependence of the relative force difference between the crystalline and the amorphous state normalized with respect to the amorphous state.

It is important to characterize the influence of the maximal number of Matsubara terms on the force. Measurements of the force were performed at separations from 40 to 140 nm. For a detailed description of the measurement see section 5.3. And it is important to know how this maximum number of terms will affect the force exactly in this range. Figure 21 shows the relative force change when one goes from 300 to 60 maximum number of additives. It is also conclusively shows that at smaller separations (less then 40 nm) one should take more Matsubara terms to get the same precision of calculations as at larger separations (above 100 nm).

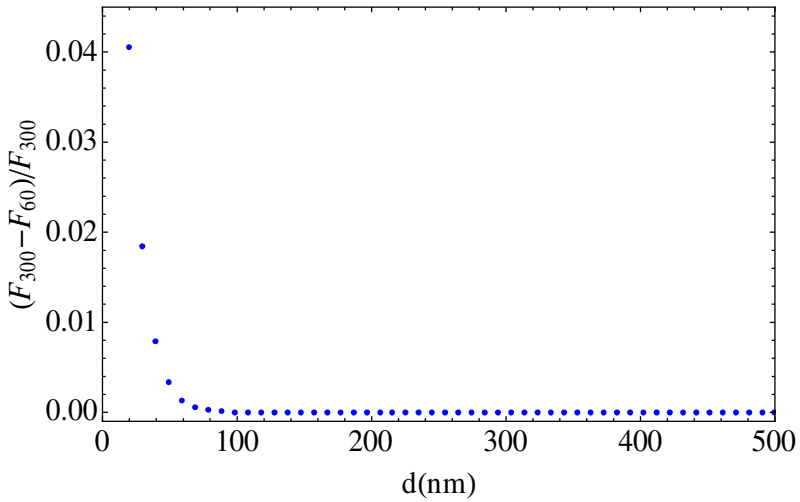

Figure 21: The relative force change between two cases of 300 and 60 maximum number of Matsubara term additives over a significant separation distance between sphere and a plate comparable to the experimental situation.

Figure 22 is a demonstrative result describing the situation with amorphous and crystalline AIST. This plot shows the relative change in dielectric response function at imaginary frequencies for the crystalline case when one skips the extrapolations. It can be seen that for the entire range of Matsubara terms the change is less then 7%. For the amorphous situation the change is even less than 3% over the entire range of Matsubara terms. This can be explained according to the fact that for the amorphous case we did not use the low frequency extrapolations, so that the error should be much less in this case. The generalized Kramers-Kronig method was also applied to AIST data, but the effect of this implementation was not able to improve the results more than 7% in a first case and 3% in the second case.

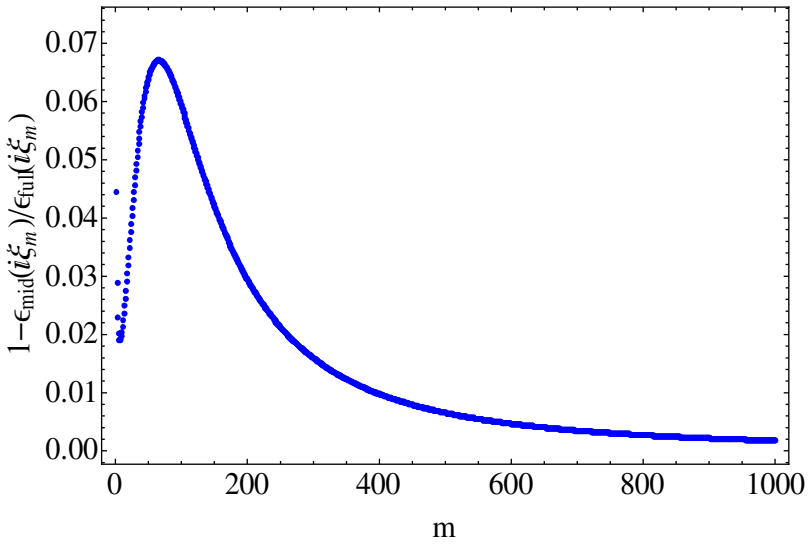

Figure 22: Effect of applying an extrapolation on dielectric response function for the crystalline AIST state. Vertical axis represents dependence of relative dielectric response function difference on number of Matsubara terms (horizontal axis).

The effect on the Casimir force was expected to be less or similar to that when one avoids the extrapolation, but it appears that applying the generalized Kramers-Kronig window function method, the force will be distorted drastically. The next two plots in figure 23 show the relative force difference when one goes from 300 number of Matsubara terms to 60 with introducing the window function for two sets of window function parameters $(p=1, q=2)$ and $(p=1, q=3)$ respectively. The generalized Kramers-Kronig method was again applied to the gold dielectric response function data. And the forces where calculated between gold sphere – crystalline AIST plate and gold sphere – amorphous AIST plate. One can see that in the desired separations from 40 to 140 nm implementation of this method to gold will lead to 15-20% error in the calculation of the force.

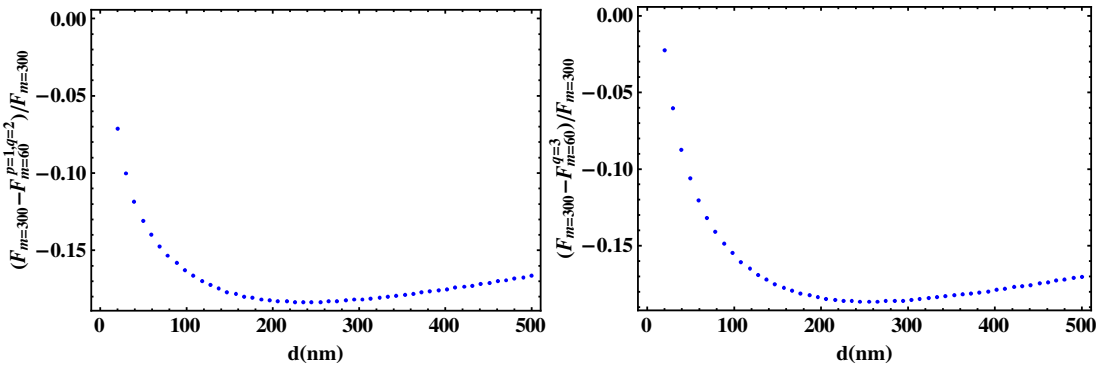

Figure 23: The relative force change between Bimonte's window function (eq. 38) with 60 Matsubara terms and trivial window function $f(z)=1$ with 300 Matsubara terms. The left side plot shows the effect on the force for the $(p=1, q=2)$ parameters set and right hand side shows it for the $(p=1, q=3)$ parameters set used in the window function.

Other values of the p, q and m parameters were also considered but they did not lead to improvement of the result. Higher values of the p and q parameters will decrease the contribution of $J_{low}^{(p,q)}(\xi)$ and $J_{high}^{(p,q)}(\xi)$ to the overall integral and will improve the result only in case of an idealized perfectly Kramers-Kronig consistent dielectric response function model. But for the real available (measured) gold data increasing of these parameter values will only lead to increase the role of the inconsistency effect on the final result. This can be explained by the oscillating behavior of the chosen form of the window function. Oscillating behavior cannot be avoided because this is needed to satisfy the analyticity of this function together with its asymptotic properties.

In conclusion, it can be said that this window method can be used with idealized perfect Kramers-Kronig consistent dielectric response function data to reduce the role of extrapolation. This work also leads to a better understanding and visualization of different frequency regions as a secondary result.

It is important to mention that when one uses the $f(z)=iz$ window function then only the real part of the dielectric response function will influence the force calculations instead of the imaginary part. In the ideal case of an analytical complex function both calculations should give the same result. However our data is not perfectly Kramers-Kronig consistent and therefore the results can differ. Thus by comparing the calculations of these two window functions one can obtain the Kramers-Kronig inconsistency characteristics. Figure 24 shows plots for the Crystalline AIST, one graph shows the difference

in dielectric function at imaginary frequencies and the other shows the difference in force. Both are plotted for m=200 number of Matsubara terms. Another interesting fact is that the $f(z)=iz$ result now becomes strongly dependent on extrapolation. In the case of $f(z)=1$ for crystalline AIST, the extrapolation affected the dielectric function on imaginary frequencies only by 4-7% (effect on the force less then 1%). But now with $f(z)=iz$ the extrapolation influences the dielectric function at imaginary frequencies more than an order of magnitude.

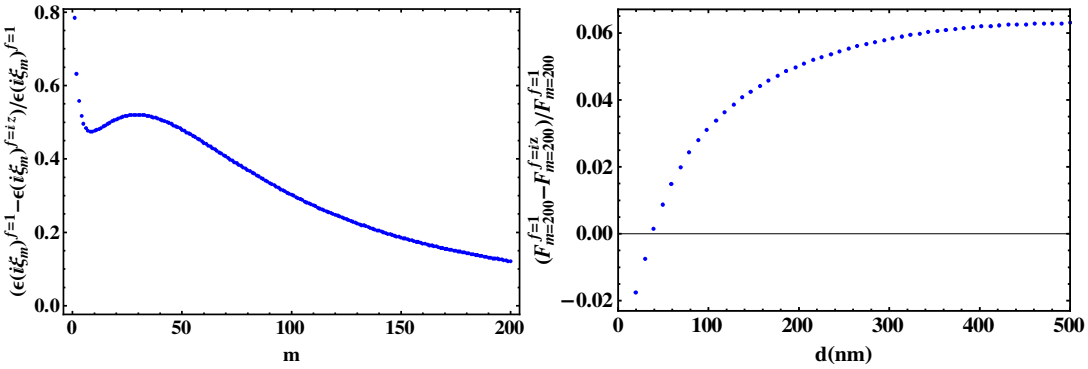

Figure 24: Calculated difference in the dielectric response function (left) and force (right) for the crystalline AIST between $f(z)=1$ and $f(z)=iz$ window functions.

5.3 Comparison with experimental results

Force measurements where performed by G. Torricelli et. al. with an ultra high vacuum (UHV) Atomic Force Microscope (AFM; an omicron VT STM) [16,17]. 100 nm thick Au coated spheres 20.2 μm in diameter were attached at the end of a cantilever. Far from the surface it initially vibrates with its resonant frequency, 83.6 kHz. When the cantilever approached the surface within the linear approximation the induced frequency shift by the sphere-plate interactions is proportional to the force gradient. The experimental force data consists of 13 measurements taken in different areas on both crystalline and amorphous PCM's samples. One should also determine the starting separation for the force measurement Z_0, the cantilever spring constant k and the contact potential difference V_0 to be able to compare the theoretical Casimir force with the measured one.

The contact potential difference was obtained and calibrated to zero value by measuring the force gradient versus separation distance for two different applied bias voltages V_b (-0.5V and +0.5V values where chosen). Generally the contact potential depends on separation distance Z between sphere and sample surface. V_0 was determined only at one distance ($Z_0 = 42.8 \pm 0.5nm$ for the amorphous and $Z_0 = 42.9 \pm 0.4nm$ for the crystalline phase sample). k and Z_0 where determined by fitting the average of these two force measurements after subtraction of the Casimir contribution. The obtained values of the spring constants are $k = 10.8 \pm 0.3N/m$ and $k = 10.7 \pm 0.3N/m$ for the amorphous and crystalline films, respectively.

Figure 25 indicates the comparison of the force calculations with the force measurements. The measured Casimir force is larger than that obtained by theory with a difference of 10-15% when the experimental standard deviation error of k and Z_0 is about 7% for both samples. But still the experimental data confirm that the Casimir force changes in magnitude of 17-22% at separations of 40-140 nm when the transition between the crystalline and amorphous state takes place (see upper inset).

One can see from this figure that the difference between the theoretical and the experimental force curves have similar behavior for both samples. This difference appears in part because the dielectric data for frequencies above $\omega > 8.86eV$ is unknown. The vertical drift of the AFM probe is excluded because the sphere plate separation Z_0 is maintained constant having the position accuracy better then ~ 1 Å. Also the roughness of the samples has an effect, and it cannot be taken into account in the theoretical calculations. The lower inset of figure 25 shows the topography of both samples. In both cases the roughness was approximately 1-2 nm, except of some localized high peaks. Although the roughness in the crystalline case was slightly higher in both cases, it is still much less then the radius of the sphere and the separation between sphere and a plate. However when one goes to smaller separations, then roughness will have a bigger effect, and this can be seen from the upper inset picture: inconsistency between theory and experiment (for the force difference between the amorphous and crystalline AIST) is higher at smaller separations.

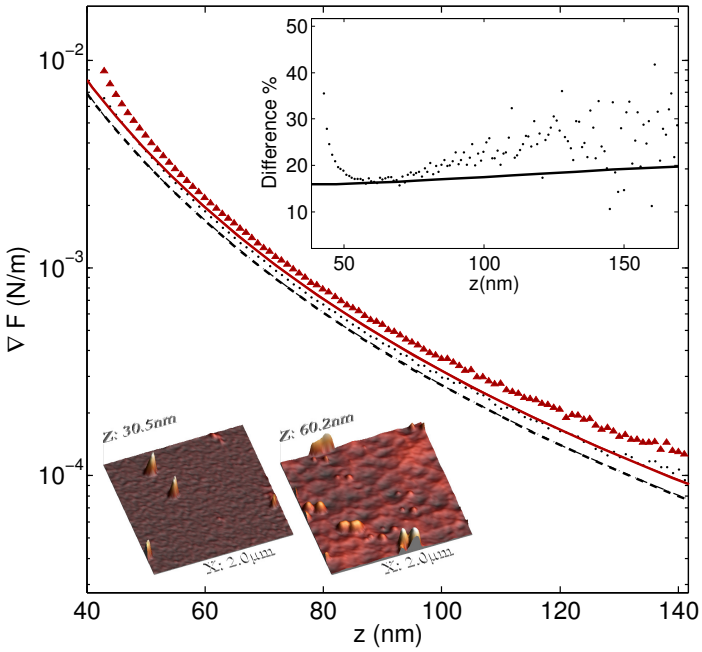

Figure 25: Red points represent the Casimir force gradient measurement for the crystalline (Δ) and amorphous (•) state. Black lines show calculated Casimir force gradient for the crystalline (—) and amorphous (---) states. The upper inset shows the experimental (•) and theoretical (—) relative difference between the two states normalized with respect to the amorphous state. The lower inset shows an AFM topography of the amorphous (left) and the crystalline (right) films. [12]

Conclusions:

The main goal of this Master thesis was to study different aspects of the theoretical calculations of the Casimir force, with emphasis on the influence of the dielectric properties on the force. Calculations have been compared to experimental results for crystalline and amorphous AgInSbTe films as probed with a gold coated sphere. The difference in Casimir force between the amorphous and crystalline states with the AIST phase change materials is the highest reported to date for a single material system and is around 20% at separations from 40 to 140 nm. The new method used here allowed us to extract much more precise results for the dielectric function in the measured range from 0.04 to 8.9 eV. This method revealed all the possible solutions and

highlighted how the analyticity principle or the Kramers-Kronig consistency works for determining the wanted physical solution. To obtain the dielectric function for the entire frequency range, Drude and Lorentz extrapolations were used. All the analyses, including optimization of these extrapolations were also performed.

Acknowledgement:

In the end I want to express my sincere gratitude to Peter van Zwoll, George Palasantzas and Bart Kooi at Zernike Institute for Advanced Materials and Vitaliy Svetovoy from MESA+ Research Institute, University of Twente whose kind consultations led me through all difficulties while doing my project.

References:

1. M. A. Ordal, L. L. Long, R. J. Bell, S. E. Bell, R. R. Bell, R. W. Alexander, Jr., and C. A. Ward. *Optical properties of the metals Al, Co, Cu, Au, Fe, Pb, Ni, Pt, Ag, Ti, and W in the infrared and far infrared*.1 April 1983 / Vol. 22, No. 7 / APPLIED OPTICS
2. *Self-consistency and sum-rule tests in the Kramers-Kronig analysis of optical data: Applications to aluminum.* Phys. Rev. B 22, 1612–1628, 1999
3. J. N. Munday, F. Capasso, V. Adrian Parsegian and S. M. Bezrukov, *Measurements of the Casimir-Lifshitz force in fluids: The effect of electrostatic forces and Debye screening.* Phys. Rev. A. 78, 032109 (2008)
4. C. J. van Oss, M. K. Chaudhury. *Interfacial Lifshitz-van der Waals and Polar Interactions in Macroscopic Systems.* Chem. Rev. 1988, 88, 927-941
5. V.B. Svetovoy, P.J. van Zwol, G. Palasantzas, and J. Th. M. De Hosson. *Optical properties of gold films and the Casimir force.* Phys. Rew B 77, 035439 (2008)
6. G.Palasantzas, V.B. Svetovoy, and P.J. van Zwol. *Influence of ultrathin water layer on the der Waals/Casimir force between gold surfaces G. Palasantzas*. Phys. Rev B 79, 235434 (2009)
7. Hiroyuki Fujiwara, *Spectroscopic Ellipsometry Principles and Applications (*Maruzen Co. Ltd, Tokyo, Japan, 2007)

8. M. Wuttig, N. Yamada, Phase-change materials for rewritable data storage. Nature Materials 7, 824–832 (2008)
9. F. Capasso, J. M. Munday, D. Iannuzzi, H. B. Chan, *Casimir forces and quantum electrodynamical torques: physics and nanomechanics.* IEEE Journal of the selected topic in quantum electronics, vol. 13. NO. 2 March/April 2007
10. H. B. G. Casimir and D. Polden, The Influence of Retardation on the London-van der Waals Forces, Phys. Rev. 73 num. 4, feb 15, 1948
11. M. Borgan, U. Mohideen, V.M. Moseoanenko, *New development in the Casimir effect.* Physics Reports 353 (2001) 1-205
12. G. Torricelli et. al., *Measurement of the Casimir effect under ultra high vacuum: Calibration method.* J. Vac. Soc. B. (To be published)
13. G. Jourdan. et. al., *Quantitave non-contact dynamic Casimir force measurements.* EPL 85 31001 (2009)
14. J. Israelachvili, *Intermolecular and Surface Forces* (Academic, New York, 1992), Vol. 2, p. 330.
15. H. B. G. Casimir, Proc. K. Ned. Akad. Wet. 51, 793 (1948)Al. W. Adamson, and A. P. Gast, *Physical Chemistry of Surfaces* (Wiley, New York, 1997), Vol. 6, p. 599.
16. T. Abe and M. L. Reed, J. Micromech. Microeng. 6, 213 (1996).
17. K. L. Ekinci and M. L. Roukes, Rev. Sci. Instrum. 76, 061101 (2005)A. Cleland, *Foundations of Nanomechanics* (Springer, New York, 2003)
18. For initial measurements of the Casimir effect see: M. J. Sparnaay, Physica (Utrecht) 24, 751 (1958); P. H. G. M. van Blockland and J. T. G. Overbeek, J. Chem. Soc. Faraday Trans. 74, 2637 (1978).
19. S. K. Lamoreaux, Phys. Rev. Lett, 78, 5 (1997).
20. G. Bressi, G. Carugno, R. Onofrio, G. Ruoso, Phys. Rev. Lett. 88 041804 (2002)
21. S. Weinberg Rev. Mod. Phys. 61 1 (1989)
22. V. M. Mostepanenko and N. N. Trunov, *The Casimir Effect and Its Applications* (Clarendon Press, Oxford, 1997); M. Bordag, U. Mohideen, and V. M. Mostepanenko, Phys. Rep. 353, 1 (2001)
23. K. A. Milton, *The Casimir Effect: Physical Manifestations of Zero-point Energy* (World Scientific, Singapore, 2001)
24. R. L. Jaffe Phys. Rev. D 72, 021301(R) (2005)
25. P. W. Milonni, *The Quantum Vacuum* (Academic, New York, 1994).
26. J. Schwinger, *Particles, Sources, and Fields I, II, and III* (Addison-Wesley, Reading, MA, 1970).
27. H. B. G. Casimir, and D. Polder, Physical Review, 73, 360 (1948)
28. S. K. Lamoreaux Phys. Today 60(2), 40 (2007)
29. R. Onofrio, New J. Phys. 8, 237 (2006).
30. R. Eisenschitz and F. London, Zeitschrift für Physik, vol. 60, p. 491 (1930). English translation in H. Hettema, *Quantum Chemistry, Classic Scientific Papers*, World Scientific, Singapore (2000).
31. E. M. Lifshitz, Sov. Phys. JETP 2, 73 (1956).

32. S. Raoux, W. Welnic, and D. Ielmini, *Phase change materials and their application to nonvolatile memories.* Chem. Rev. 2010, 110, 240-267
33. F. Pinto, *Engine cycle of an optically controlled vacuum energy transducer*. Phys. Rev. B vol. 60, num. 21, 1999
34. G. Bimonte, *A generalized Kramers-Kronig transformation for Casimir effect computations*, Phys. Rev. A, 2010